Implications of the 9 July 1956 M_S ~ 7.2 Amorgos Earthquake for Tsunami Hazard in the Aegean

Nikos Kalligeris[1] , **Costas Synolakis[2,3]**, **Philip England[4]** , **James Jackson[5]** , and **Richard Walker[4]**

[1]Institute of Geodynamics, National Observatory of Athens, Athens, Greece, [2]Academy of Athens, Athens, Greece, [3]Viterbi School of Engineering, University of Southern California, Los Angeles, CA, USA, [4]Department of Earth Sciences, University of Oxford, Oxford, UK, [5]Department of Earth Sciences, Bullard Labs, Cambridge, UK

Abstract The 9 July 1956 Amorgos earthquake was followed by sea waves that affected a large part of the southern Aegean Sea and, in places, were higher than 10 m. Previous analyses of this event concluded that waves generated directly by co-seismic displacement of the seafloor were small in comparison with those caused indirectly by localized submarine landsliding. Seismological and geodetic evidence, combined with marine geophysical and submarine surveys, indicate that coseismic seafloor displacements exceeded by an order of magnitude those assumed in previous studies. Detailed calculations of runup are possible for 25 sites; with the exception of one island, these agree with observations to within uncertainty, suggesting that co-seismic displacement of the seafloor was the principal cause of the 1956 tsunami. Scenarios of tsunami hazard from future earthquakes in the Aegean should take into account the large ratio of displacement to fault length in this earthquake.

Plain Language Summary The 1956 Amorgos earthquake was followed by a tsunami that reached heights of several meters up to 100 km from the earthquake, and of 10 m and more on islands nearby. Whereas tsunamis following large earthquakes are usually the direct result of displacement of the seafloor by the earthquake, flooding during the 1956 tsunami was attributed to submarine landslides triggered by the shaking. If that interpretation is correct, assessment of tsunami hazards associated with future earthquakes in the Aegean becomes problematic, because triggered landsliding can occur far from the location of the earthquake, and is very hard to predict. We reassess the seismological evidence and show that the 1956 tsunami dropped the seafloor by 5–8 m in a 40–50-km swath along the SE coast of Amorgos. Our calculations of the resultant tsunami and onshore flooding show close agreement with what was observed at the time. We therefore conclude that most of the flooding in 1956 was caused by displacement of the seafloor during the earthquake, not by landsliding. Assessment of future tsunami hazard of the region should take into account the likelihood that the unusually large displacements in the 1956 earthquake may be repeated in future earthquakes of the region.

1. Introduction

The 9 July 1956 M_S ~ 7.2 Amorgos earthquake, one of the largest to have occurred within the Aegean Sea during the instrumental period, was followed by a tsunami that affected the shorelines of many islands within the Aegean, as well as the coasts of Crete and western Turkey. Waves reaching 1–3 m above undisturbed sea level were reported from over 60 locations and, on Amorgos and neighboring islands, exceeded 10 m (Okal et al., 2009, and Figure 1). In what follows, we use "runup" as the general term to refer to tsunami intensity (usage as in the UNESCO Tsunami Glossary UNESCO-IOC (2019)); use of detailed terminology describing transient water height above undisturbed sea level is confined to Section 3, where it is needed for discussion of quantitative comparison between calculation and observation.

Previous studies adopted a depth of 45 km or greater for the earthquake with the consequence that amplitudes of seafloor displacement and the associated wave heights were calculated to be a few tens of centimeters, much smaller than the observed runups (e.g., Okal et al., 2009, Figures 7 and 9). Local submarine landsliding was considered to account for the scale and lateral variation of the observed runups (Ambraseys, 1960; Galanopoulos, 1957; Okal et al., 2009). We present several lines of evidence which, to the contrary, point to a causative fault that broke the seafloor, generating sea–floor displacements an order of magnitude larger than considered in earlier studies (e.g., Ambraseys, 1960; Okal et al., 2009). We calculate the propagation and runup of tsunamis based upon those displacements and find agreement with the runups observed in 1956.

Writing – original draft:
Nikos Kalligeris, Costas Synolakis,
Philip England
Writing – review & editing:
Nikos Kalligeris, Costas Synolakis,
Philip England, James Jackson,
Richard Walker

2. Parameters of the 9 July 1956 $M_S \sim 7.2$ Amorgos Earthquake

Calculation of tsunami generation and propagation requires knowledge of the disturbance to the seafloor, and its relation to the surrounding bathymetry and topography. Previous estimates of epicentral location for the earthquake differ by a few tens of kilometers, which is greater than the typical spacing between faults of the region (e.g., Hooft et al., 2017; Tsampouraki-Kraounaki et al., 2021, and see Figure 1b). Estimates of the depth of faulting vary from <15 to >45 km (Table S1 in Supporting Information S1), and estimates of scalar moment vary from 4–7×10^{19} N m (Brüstle et al., 2014) to 3×10^{20} N m (Okal et al., 2009) with a consequent large uncertainty in the magnitude of seafloor displacement. In this section we combine seismological, geomorphological, and geodetic data to constrain the location and magnitude of that displacement.

2.1. Causative Fault

An obvious candidate for the fault that slipped in the 1956 earthquake is the Amorgos Fault, which runs along the SE coast of the island, and is marked by between 1 and 2 km of relief, which includes a submarine scarp of approximately 700 m (e.g., Ambraseys & Jackson, 1990; Nomikou et al., 2018; Papadopoulos & Pavlides, 1992; Stiros et al., 1994, and see Figures 1b and 4). However, given the uncertainties in hypocentral location and the proximity of other major normal faults, the prominence and steepness of the southeast slope of Amorgos are not, alone, sufficient to confirm that the 1956 earthquake was located on this feature (e.g., Tsampouraki-Kraounaki et al., 2021, Section 5.3).

Three independent observations, from locations shown in Figure 2b, greatly strengthen the case for the Amorgos Fault as being the causative fault for the 1956 earthquake. At the northeastern end of the footwall of the Fault, a late-19th-century triangulation monument shows a displacement, relative to the neighboring islands, of 1.2 ± 0.15 m which, as we show in Section S2 in Supporting Information S1, requires slip of 5 m on a fault passing close to the monument. Near the middle of the SE coast of Amorgos, Stiros et al. (1994) observed a marine bench at about 40 cm above sea level which they interpreted, from its morphology, from comparison of pre-and-post-1956 aerial photographs, and from radiometric dating of a vermetid recovered from the bench, as recording uplift of the footwall during the 1956 earthquake. Third, recent exploration with ROVs (Leclerc et al., 2024) at a location about 5 km SW of the observations of Stiros et al. (1994) (Figure 2) revealed a striated fault surface along a 500-m section on the bathymetric scarp which they interpreted as being caused by the 1956 earthquake.

For the purposes of our hydrodynamical calculations, we consider three sections of fault (F1, F2, and F3, Figures 1 and 2). F1 and F2 correspond to the Amorgos Fault, and segment F3 to the Amorgos North Relay Fault (nomenclature of Tsampouraki-Kraounaki et al. (2021), Figure 9). The cumulative vertical offset on F1 and F2 is similar to that on F3 (2 km, Tsampouraki-Kraounaki et al., 2021). The combined length of the three segments is about 45 km; an earthquake of M_W 7.2 will typically involve a fault length of about 40–50 km, so it is reasonable to investigate the possibility that all three segments slipped in the earthquake.

2.2. Depth Extent of Faulting

Okal et al. (2009) modeled surface waves of periods 100–200 s and obtained a depth of 45 km for the centroid, inferring a maximum depth of faulting in excess of 60 km. Brüstle et al. (2014) modeled the waveforms of body waves at three stations that recorded the earthquake; their best fit had a centroid depth of ~20 km. Leclerc et al. (2024) argued that slip in the earthquake penetrated to the base of the crust at a depth of 25 km. Those depths are, however, inconsistent with what is known of the depth extent of large earthquakes in the Aegean during the past 60 years, from body-wave modeling, from aftershock studies, and from interferometric synthetic aperture radar studies, all of which indicate that the thickness of the seismogenic layer in this region is unlikely to exceed 15 km (Baker et al., 1997; Bernard et al., 1997; Hatzfeld et al., 1995, 1997, 2000; Jackson et al., 1982; Meyer et al., 1996; Resor et al., 2007; B. Shaw & Jackson, 2010; Taymaz et al., 1991). In particular, geodetic and seismic studies of recent tsunamigenic earthquakes in the eastern Aegean region (the 2017 Bodrum-Kos earthquake (Ganas et al., 2019; Karasözen et al., 2018), and the 2020 Samos earthquake (Karakostas et al., 2021; Lentas et al., 2022), marked as KB and S on Figure 1a) showed rupture confined to the upper 10–15 km of the crust.

We therefore carry out our hydrodynamical calculations under the assumption that rupture in the Amorgos earthquake penetrated no deeper than 15 km, as was the case for the other large normal-faulting events of the region whose rupture depth is constrained. This assumption is also consistent with recent measurements of
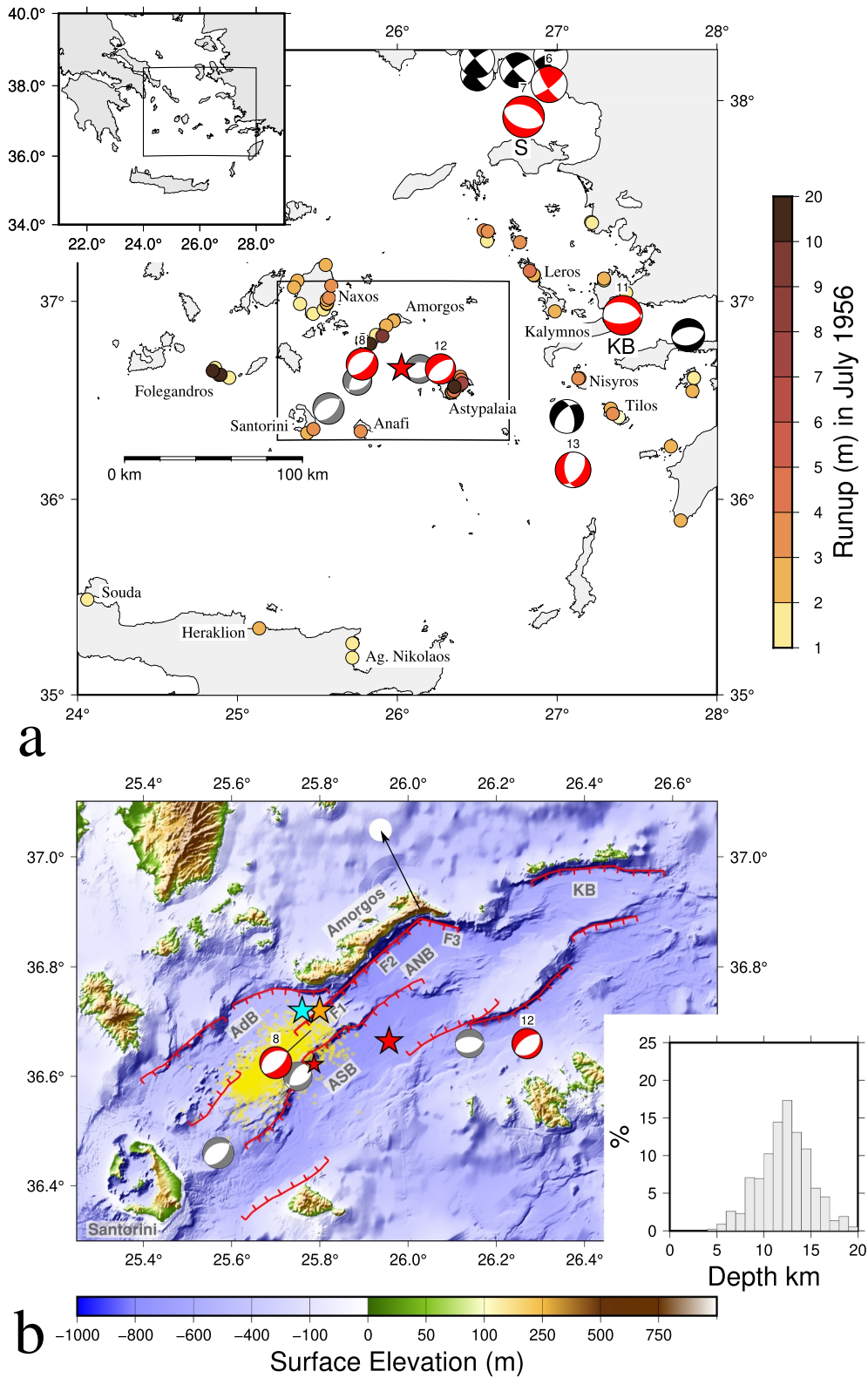
Figure 1.

microseisms in the region (e.g., Andinisari et al., 2021; Bohnhoff et al., 2006; Ganas et al., 2012; Kassaras et al., 2014, 2022), and with the hypocenters of a burst of earthquakes between Amorgos and Santorini which occurred in late January and February 2025 (Figure 1).

2.3. Dip of the Faults

The seismic profiles of Nomikou et al. (2018) and Tsampouraki-Kraounaki et al. (2021) show that, in the upper few kilometers, the Amorgos Fault dips at ∼50°–60° to the SE, and that the Amorgos North Relay Fault dips to the SSW at 45°–50°. A southeasterly dip of about 60° is consistent with the focal mechanisms of Shirakova (reported by Okal et al. (2009)) and Brüstle et al. (2014) (Table S1 in Supporting Information S1), and with the submarine observations reported by Leclerc et al. (2024). The much lower dip (∼25°) suggested by Okal et al. (2009) for the SE-dipping plane is inconsistent with the seismic profiles.

The result of the hydrodynamic calculations are heavily dependent on the vertical component of the slip, which is uncertain by more than a factor of 2 (Section 2.4), but relatively insensitive to uncertainty in dip or rake. Therefore, for simplicity of presentation, we use a dip of 60° and assume that slip was in the down–dip direction (rake −90°).

2.4. Magnitude of Slip

We estimate the magnitude of slip in the earthquake by dividing its scalar moment by the shear modulus and the area of the fault that slipped. Okal et al. (2009) estimated the moment to have been 3.9×10^{20} N m. Ambraseys (2001) re-assessed the surface-wave magnitude for the earthquake, and determined a range of $M_S = 7.2 \pm 0.2$ which, using the M_S–M_0 relations of Ekström and Dziewonski (1988), converts to a range of 0.4–2×10^{20} N m for the scalar moment. The difference between this range and the estimate of Okal et al. (2009) may be explained by the diminishing excitation of surface waves with earthquake depth: Okal et al. (2009) employed a centroid depth of 45 km, whereas Ambraseys (2001) used a depth of 15 km which is consistent with the range of depths discussed in Section 2.2.

The combined length of segments F1 and F2 is 35 km, and the length of F3 is 11 km. For a dip of 60°, and a maximum depth of 15 km for the rupture, the area of slip is between 600 and 800 km^2. For a shear modulus of 3.3×10^{10} N m^{-2}, the magnitude of slip for $M_S = 7.2$ ($M_0 \sim 10^{20}$ N m) is ∼3–5 m. Taking account of uncertainties at least 0.2 in M_S (Ambraseys, 2001), which are equivalent to a factor of two in moment, we allow an average slip range from 4 to 12 m for the smaller fault area (F1 + F2), and 2–8 m for the three fault segments combined (Table 1). Leclerc et al. (2024, Table S4) show mean displacements of 13 m from a 300-m section of the submarine fault trace (location L in Figure 2); the minimum offset observed was 9.8 m but it is unclear how much of that displacement is due to slumping or compaction of the poorly consolidated sediment of the hanging wall.

3. Tsunami Calculations

Okal et al. (2009, Table 2 and Figure 8) reported interviews of eyewitnesses to flooding following the 1956 earthquake, which were carried out between 2003 and 2007 using methods described by Synolakis and

Figure 1. Setting of the 9 July 1956, $M_S \sim 7.2$ Amorgos earthquake and tsunami. (a) Regional setting. Box within inset shows location of the main figure; box within main figure shows the location of panel (b). Red star shows the ISC-GEM epicenter of the 1956 earthquake (Bondãr et al., 2015). Colored circles (scale to right) show runups from the subsequent tsunami (Okal et al., 2009, Table 2 and Figure 8). Mechanisms of other earthquakes are from the Global CMT catalog (Dziewonski et al., 1981; Ekström et al., 2012, $M_W \geq 5.5$ black fill and $M_W < 5.5$, gray fill), and from long-period-body-wave modeling (B. Shaw & Jackson, 2010; Taymaz et al., 1991, and Section S1 in Supporting Information S1, red fill). KB and S mark the mechanisms of the tsunamigenic 2017 Kos-Bodrum and 2020 Samos earthquakes. Numbers above mechanisms with red compressional quadrants show centroid depth in km. (b) Local setting. Topography and bathymetry of the region are shaded with illumination from the north-west; topography from SRTM data (Farr et al., 2007) and bathymetry from EMOD (EMODnet, 2022). Red, cyan, and orange stars show the epicenters for the main shock given, respectively, by Bondãr et al. (2015), Ambraseys (1960), and Okal et al. (2009). Smaller red star shows the epicenter of the largest aftershock (Bondãr et al., 2015). Black arrow with error ellipse shows the orientation of a 1.2 ± 0.15-m displacement of a geodetic monument on the crest of Amorgos, which probably occurred in the earthquake (Section S2 in Supporting Information S1). The normal-fault segments F1–F3 used in the tsunami calculation (Section 3) are shown by the thicker red lines with ticks on the down-thrown sides. Thinner ticked lines show the locations of other faults identified by Nomikou et al. (2018) and Tsampouraki-Kraounaki et al. (2021) on the basis of prominent bathymetric scarps. Labels AdB: Anydros Basin, ANB: Amorgos North Basin, ASB: Amorgos South Basin, and KB: Kinairos Basin use the nomenclature of Tsampouraki-Kraounaki et al. (2021). Yellow dots show epicenters of $M_L \geq 3$ earthquakes located by the National Observatory of Athens between 27 January 2025 and 20 February 2025; histogram to right shows distribution of their depths (https://gein.noa.gr/en, accessed 27 April 2025).
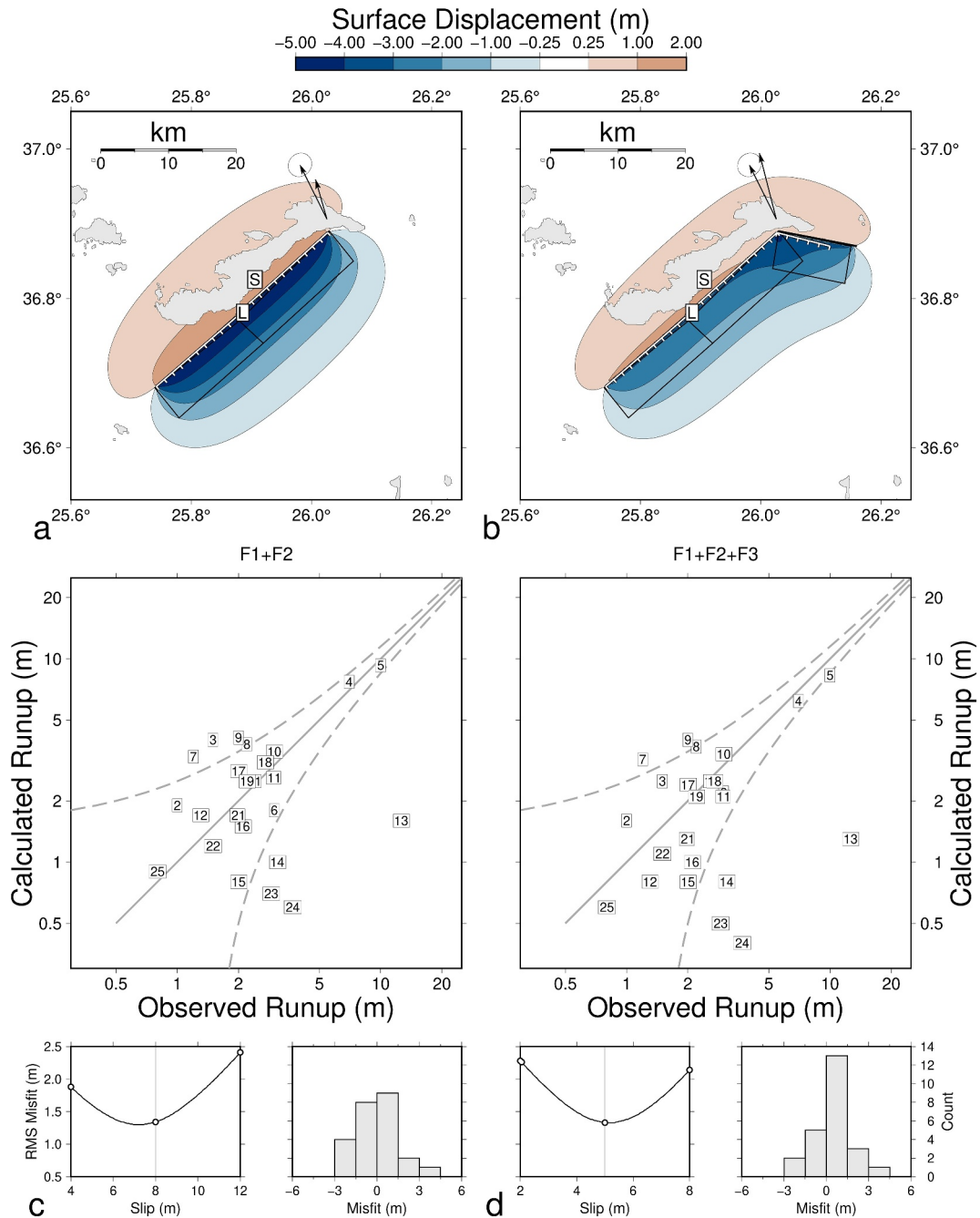
Figure 2. Sea-floor displacements in the 1956 Amorgos earthquake, and the associated tsunami runups. (a, b) Vertical displacements of seafloor. The three contiguous fault segments are defined by the four bounding points (25.742°E, 36.682°N: F1), (25.875°E, 36.775°N: F1 and F2), (26.027°E, 36.888°N: F2 and F3), and (26.155°E, 36.870°N: F3); all dip at 60° and their rakes are −90°. (a) Vertical displacements for slip of 8 m on each of the fault segments F1 and F2. Arrows with error ellipse shows horizontal displacement by 1.2 ± 0.15 m of 1890s triangulation monument (Figure S2 in Supporting Information S1); arrow without ellipse shows calculated horizontal displacement of that point due to slip on the dislocations. S, location of footwall uplift discussed by Stiros et al. (1994). L, location of the fault mirror described by Leclerc et al. (2024). (b) As for (a), with slip of 5 m on each of segments F1, F2, and F3. (c, d) Comparison between observed and calculated runups for displacements shown in panels (a, b). Solid gray lines denote exact fit; dashed lines represent misfits of ±1.5 m. Lower left panels show variation of root-mean-square misfits (excluding point 13) as slip on the faults varies; circles show calculations for minimum, mean, and maximum slips listed in Table 1, lines show interpolations assuming linear relation between slip and runup. Lower right panels show distributions of misfits.

Table 1
Comparison Between Observed and Calculated Inundation Height/Runup for the Two Configurations of Faulting Shown in Figures 2a and 2b

	Island	Longitude (°E)	Latitude (°N)	Obs.	F1 + F2 4 m	F1 + F2 8 m	F1 + F2 12 m	F1 + F2 + F3 2 m	F1 + F2 + F3 5 m	F1 + F2 + F3 8 m
1	Amorgos[a]	25.9771	36.9016	2.5	1.2	2.5	3.4	1.1	2.5	3.9
2	Amorgos[b]	25.9781	36.9043	1.0	1.0	1.9	3.0	0.8	1.6	2.3
3	Amorgos[b]	25.8672	36.8308	1.5	2.4	4.0	5.4	1.1	2.5	3.5
4	Astypalaia[b]	26.3561	36.5704	7.0	3.8	7.7	11.7	2.7	6.2	11.2
5	Astypalaia[b]	26.3575	36.5704	10.0	4.9	9.3	15.7	3.3	8.3	11.5
6	Astypalaia[b]	26.3942	36.6205	3.0	1.1	1.8	2.8	0.9	2.2	2.6
7	Astypalaia[a]	26.3896	36.5769	1.2	2.1	3.3	4.2	1.6	3.2	4.5
8	Astypalaia[b]	26.3850	36.5767	2.2	2.3	3.8	4.8	1.7	3.7	5.1
9	Astypalaia[b]	26.3837	36.5754	2.0	2.5	4.1	5.2	2.0	4.0	5.7
10	Astypalaia[b]	26.3832	36.5742	3.0	2.0	3.5	4.4	1.5	3.4	4.7
11	Anafi[a]	25.7711	36.3446	3.0	1.2	2.6	4.1	0.8	2.1	3.0
12	Folegandros[b]	24.9482	36.6155	1.3	0.9	1.7	2.5	0.4	0.8	1.3
13	Folegandros[b]	24.8941	36.6309	12.6	0.8	1.6	2.3	0.5	1.3	2.2
14	Folegandros[b]	24.8846	36.6302	3.1	0.6	1.0	1.7	0.4	0.8	1.3
15	Naxos[a]	25.3749	37.1038	2.0	0.5	0.8	1.1	0.3	0.8	1.2
16	Naxos[b]	25.3539	37.0701	2.1	0.8	1.5	2.4	0.5	1.0	1.6
17	Leros[a]	26.8542	37.1312	2.0	1.5	2.8	3.7	1.0	2.4	3.4
18	Leros[b]	26.8527	37.1324	2.7	1.5	3.1	4.3	1.0	2.5	4.0
19	Kalymnos[a,c]	26.9823	36.9493	2.2	1.5	2.5	3.2	1.0	2.1	2.7
20	Crete, Souda[b]	24.0608	35.4889	1.5	0.7	1.2	1.5	0.4	1.1	1.2
21	Crete, Heraklion[b]	25.1359	35.3417	2.0	0.8	1.7	1.9	0.6	1.3	1.7
22	Crete, Ag. Nikolaos[b]	25.7189	35.1907	1.5	0.6	1.2	1.6	0.4	1.1	1.6
23	Nisyros[b]	27.1385	36.6139	2.9	0.3	0.7	1.0	0.1	0.5	0.8
24	Nisyros[b]	27.1322	36.6117	3.7	0.3	0.6	1.0	0.2	0.4	0.7
25	Tilos[a]	27.3856	36.4168	0.8	0.4	0.9	1.3	0.2	0.6	0.9

Note. See Figure 1 for the locations of islands named here. [a]Inundation height. [b]Runup. [c]This data point has been updated, because there appears to have been a transcription error in Table 2 of Okal et al. (2009); the location here is in agreement with the description in the text of Okal et al. (2009), and with the memory of the second author of both this and the original paper, who carried out the interview.

Okal (2005). The reports of flooding fall into two categories. One is the inundation height, the height above undisturbed sea level to which a specific location (usually a building or harbor wall) was flooded; the other is the runup, the height above the sea level of the furthest inland point to which the flooding reached (usage as in the UNESCO Tsunami Glossary UNESCO-IOC (2019)). We have expressed the observations of Okal et al. (2009) in those terms, cross-checking when necessary with the original field notes. Elevations were measured with hand level and survey rod, and the tidal range in all locations is less than 30 cm; uncertainties in runups measured in this way are at the level of ~50 cm.

We make quantitative comparison between the reported elevations and calculations of tsunami inundation based on the fault models described in the previous section. The prerequisite for such calculation is the availability of bathymetric and topographic data for the near-shore environment at a spatial resolution of ~10 m or less (e.g., Behrens et al., 2021). Bathymetric surveys of that resolution do not exist for many of the locations at which runups were reported; detailed comparison is therefore restricted to the 25 locations given in Table 1, for which such data are available.

We calculate tsunami elevations using the hydrodynamic model MOST (Titov & Synolakis, 1995, 1998; Titov et al., 2016) through the ComMIT interface (Titov et al., 2011); the procedure and details relevant to the present study are given in Section S3 in Supporting Information S1. Although MOST does not calculate frequency dispersion of waves, that process has negligible influence on wave heights within the Cyclades; there may be a minor influence on waves traveling to the three most distant sites, in Crete (see Glimsdal et al. (2013), and discussion of Section S3 in Supporting Information S1).

The initial condition for each calculation is provided by the seafloor displacements corresponding to the relevant configuration of faulting and slip (Figures 2a and 2b) which are obtained using the method of Okada (1992). Maximum wave heights for slip of 8 m on faults F1 + F2 and 5 m on faults F1 + F2 + F3 after 5 hr propagation simulations on GEBCO bathymetry (GEBCO Compilation Group, 2024) are shown in Figure 3. The greatest concentration of wave energy is beamed perpendicular to the source, toward Amorgos and Astypalaia. This feature is commonly observed for seismic tsunamis because the speed of wave propagation is much lower than that of fault rupture, resulting in positive interference, in the direction perpendicular to the fault strike, between waves from different parts of the source. Details of distribution of maximum wave height reflect the complexity in bathymetry. Maximum wave heights for the other sources of Table 1 are shown in Figure S4 in Supporting Information S1.

Table 1 lists the maximum calculated value of runup or inundation height at each location for the six configurations of faulting modeled. Comparison between calculated and observed values for slip of 8 m on faults F1 + F2, and of 5 m on faults F1 + F2 + F3 are shown in Figures 2c and 2d. Although the hydrodynamical calculations are non-linear, runups for each location are proportional, to within 10%, to the magnitude of the slip for a given fault model. We can therefore infer the variation of misfit with the magnitudes of slip on the fault systems. With point 13 excluded (see below) the minimum RMS misfit for the F1 + F2 calculations is 1.30 m at a slip of 7.2 m and for faults F1 + F2 + F3 it is 1.33 m at 5.2 m of slip (lower-left panels, Figures 2c and 2d). RMS misfits remain smaller than 1.5 m while slip on F1 + F2 is in the range 5.4–9.0 m and, for F1 + F2 + F3, in the range 4.0–6.4 m.

Misfits to observations lie within ±1.5 m in 17/25 cases for the 2-segment calculation (Figure 2c) and in 18/25 cases for the 3-segment calculation (Figure 2d). The misfit of 11 m for point 13 on Folegandros is, however, a clear outlier; it cannot be explained by faulty memory, measurement error, or errors in bathymetry; nor can a splash of 15 m (point 27 of Okal et al. (2009)) reported from a nearby location where bathymetric data at the resolution necessary for calculation of runup do not exist. We consider, as did Okal et al. (2009), that runups at point 13 and perhaps others on the south coast of Folegandros were influenced by localized landsliding.

Okal et al. (2009) also attributed the runups of 9.7 and 20 m on the SW coast of Amorgos to landsliding, because of their magnitudes and large variation over a short distance (Figure 4). There are no high-resolution bathymetric data for this coast, so we calculate wave heights with the same sources as used for Figure 2, but with the intermediate-resolution bathymetric data (B grids of Section S3 in Supporting Information S1). Following a common approach when detailed bathymetry is unavailable, wave heights at the 50-m isobath are converted into an approximate estimate of inundation height at the coast using the rule proposed by Green (1838) which, assuming conservation of wave energy, relates wave heights w_0, w_1 at water depths d_0, d_1 by

$$w_1 = w_0 \left(\frac{d_0}{d_1}\right)^{1/4} \tag{1}$$

(Green, 1838, Equation 5). Estimated near-shore inundation heights with $d_1 = 1$ m (as suggested, e.g., by Hébert and Schindelé (2015) and Selva et al. (2021)) are shown in Figure 4.

Along the SE coast of Amorgos estimated inundation heights are between ∼5 m and over 15 m, with significant variations occurring on the horizontal scale of a few kilometers (Figures 4b and 4d). The magnitudes of the waves, and their lateral variability, are explained by the proximity of 5–8 m vertical displacements of sea-floor (Figures 2a and 2b) to a submarine scarp of ∼700 m (Figures 4a and 4c (and see Leclerc et al., 2024)). The waves are amplified in embayments, such as at Mouros (8 km on Figures 4b and 4d) and Agia Anna (16 km) where the runups of 20 and 9.7 m, respectively, were reported by Okal et al. (2009, Table 2). At each of those locations, the range of estimated inundation heights encompasses the reported runup.
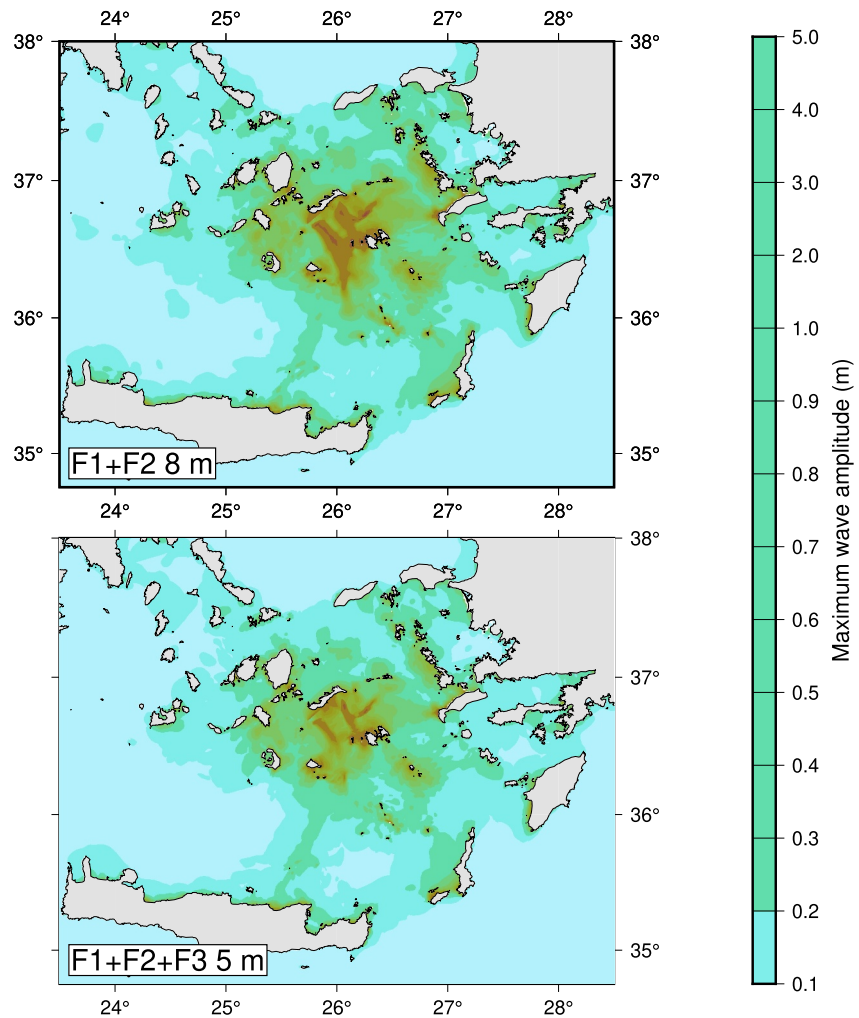
Figure 3. Hydrodynamic calculations of maximum wave heights (above undisturbed sea level) for slip of 8 m on faults F1 + F2 and 5 m on faults F1 + F2 + F3 Figure 2. Colors (scale at side) display the maximum height of the sea surface above its undisturbed level in the 5 hr following the earthquake.

We conclude, from the agreement between calculated and observed runups (Figure 2), and between the estimated and observed runups of 10–20 m on the SE coast of Amorgos (Figure 4), that the co-seismic displacements of the seafloor during the 1956 Amorgos earthquake produced a tsunami that accounts for the principal features of the observed inundation, with the exception of that on the southwest coast of Folegandros.

4. Discussion

The magnitudes of slip required to fit the runups observed in 1956 are very similar to the average slips estimated in Section 2.4 for an earthquake of scalar moment 10^{20} N m. Although the ratio of slip to fault length (~ 1–2×10^{-4}) is at the high end of the range observed for normal-faulting earthquakes (e.g., Henry & Das, 2001; B. E. Shaw & Scholz, 2001; Wells & Coppersmith, 1994), it is comparable with those observed for other large continental normal-faulting earthquakes, for example, the 1954 Fairview Peak, Nevada, 1959 Hebgen Lake, Montana, and 2008 Yutian, Tibet, earthquakes (Elliott et al., 2010; Johnson et al., 2018; Savage & Hastie, 1966), the historic Huaxian earthquake (Feng et al., 2020), and the proposed prehistoric Egiin Davaa event in Mongolia (Walker et al., 2017). The comparisons of runup (Figure 2) cannot distinguish between the smaller slip on the longer fault system and the larger slip confined to the two fault segments along the SE coast of Amorgos, but comparison with the large continental earthquakes slightly favors the former. Slips in the M7.1 to 7.2 Fairview Peak, Hebgen Lake, and Yutian earthquakes, rupture lengths ~30–40 km, were approximately 4 m whereas the slips of ~8 m in the Huaxian and Egii Davaa took place on faults about 80 km in length.
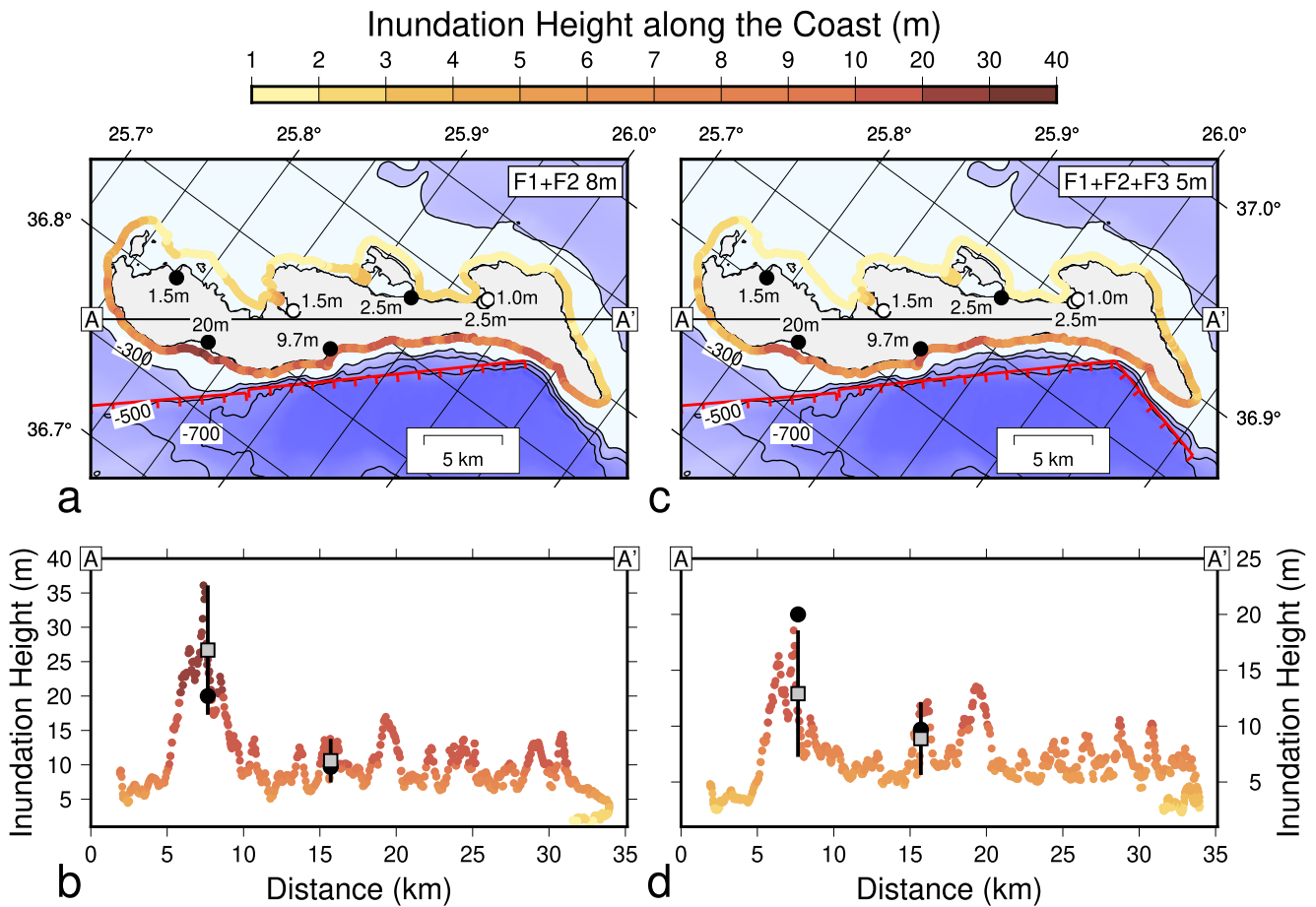
Figure 4. Estimate of inundation height along the coastline of Amorgos following the 1956 earthquake, calculated from intermediate-resolution bathymetry. (a) Inundation heights (color scale at top) are shown at the location of the 50-m bathymetric contour from which they were calculated (Equation 1). Circles, labeled with heights in meters, show locations of runup reported by Okal et al. (2009); sites included in Table 1 are shown as circles with white fill. Bathymetry shown by contours and shades of blue. Locations of faults F1 and F2 shown in red. Line A-A′ shows orientation of profile shown in panel (b). (b) Colored points show estimates of inundation height along the SE coast (Equation 1), for 8 m of slip on faults F1 + F2; distances are measured along the profile shown in panel (a). Black dots show observations; gray squares, with error bars show the centers, and ranges, of the estimated inundation heights within 500 m of the observation points. (c, d) As for (a, b), but for 5 m of slip on faults F1 + F2 + F3.

The large slip in the 1956 Amorgos earthquake has implications for assessments of tsunami hazard if a submarine earthquake were to occur in the region, because the estimation of runup depends critically on the magnitude of slip in the earthquake. Tsunami hazard assessment studies and tsunami forecasting (in the absence of additional information to constraint slip) often employ scaling relations to infer source rupture parameters, including slip magnitude. Several studies have emphasized that empirical scaling relations introduce significant epistemic uncertainty in both deterministic and probabilistic assessments of tsunami hazard (e.g., Behrens et al., 2021; Satake et al., 2022). To illustrate this point, let us apply as an example the moment-slip scaling of Leonard (2014, Equation 11) to the moment of the 1956 event (0.5–2×10^{20}, Ambraseys, 2001). This yields slip estimates between 1 and 1.5 m, which underestimate, by a factor of five or greater, the slip that actually occurred and, if used to calculate tsunami hazard, would underestimate tsunami wave heights for this case by the same factor.

5. Conclusions

The 1956 Amorgos earthquake involved slip of between 5 and 8 m on the Amorgos Fault, and perhaps also on the Amorgos North Relay fault, with rupture extending from a depth of ~15 km to the surface. Hydrodynamical calculations demonstrate that the tsunami generated by displacement of the seafloor during the earthquake was

responsible for the runups of over 1 m up that were observed up to 100 km from the epicenter, and for runups of 5–20 m in the near field (Figures 2 and 4). There is no need to invoke widespread submarine landslides, as had previously been suggested (e.g., Ambraseys, 1960; Galanopoulos, 1957; Okal et al., 2009), although localized landsliding triggered by the earthquake remains a likely explanation for runup greater than 10 m on the south coast of Folegandros.

Assessment of the tsunami hazard from future earthquakes in the Aegean should take into account the fact that, as in other large normal-faulting continental earthquakes, the ratio of slip to fault length ($\sim$1–2 $\times$ 10^{-4}) was considerably greater in this earthquake than is given by the scaling relations commonly used to relate fault length to earthquake magnitude.

Data Availability Statement

Supporting Information S1 for this paper is archived at Kalligeris et al. (2025). The runup data used in our analysis are given in Table 1. The previously unpublished earthquake focal mechanisms and centroids depths, shown in Figure 1 and listed in Table S1 in Supporting Information S1, were obtained by analysis of digital waveforms downloaded from the Incorporated Research Institutions for Seismology (IRIS) Consortium at https://ds.iris.edu/wilber3/find_event, as described in Section S1 in Supporting Information S1 (Figures S1 and S2 in Supporting Information S1). Displacements of 1890s triangulation monuments used in Section S2 in Supporting Information S1 are given in Davies et al. (1997, Table 1).

Bathymetric and topographic data used for hydrodynamical calculations of tsunami propagation are from EMODnet (EMODnet, 2022), GEBCO (GEBCO Compilation Group, 2024) and the European Digital Elevation Model (EU-DEM, version 1.1, available through https://www.gpxz.io/blog/eudem; last access: 3 March 2025). Nearshore bathymetric data used in calculations of runup were obtained by digitizing nautical charts available from the Hellenic Navy Hydrographic Service (https://hnhs.gr/en/product-category/nautical-charts/), nautical charts XEE 360/3, 423/1, 423/4, 423/5, 423/7, 424/2, 424/3, 433/1, 443/1, 444/1, 451/1, and 451/2. Topographic data at 5 m may be requested from the Hellenic Cadastre (https://gis.ktimanet.gr/geoportal/catalog/search/resource/details.page?uuid=%7B456CB655-B899-450A-87BF-8322B8FB8370%7D).

The hydrodynamical software used in this research, ComMIT (which includes MOST) is available through the dedicated website hosted by the National Oceanic and Atmospheric Administration (NOAA) of the USA: https://nctr.pmel.noaa.gov/ComMIT/.

References

Ambraseys, N. N. (1960). The seismic sea wave of July 9, 1956, in the Greek archipelago. *Journal of Geophysical Research*, *65*(4), 1257–1265. https://doi.org/10.1029/jz065i004p01257

Ambraseys, N. N., & Jackson, J. (1990). Seismicity and associated strain of central Greece between 1890 and 1988. *Geophysical Journal International*, *101*(3), 663–708. https://doi.org/10.1111/j.1365-246x.1990.tb05577.x

Ambraseys, N. N. (2001). Reassessment of earthquakes, 1900–1999, in the eastern Mediterranean and the Middle East. *Geophysical Journal International*, *145*(2), 471–485. https://doi.org/10.1046/j.0956-540x.2001.01396.x

Andinisari, R., Konstantinou, K., & Ranjan, P. (2021). Seismicity along the Santorini-Amorgos zone and its relationship with active tectonics and fluid distribution. *Physics of the Earth and Planetary Interiors*, *312*, 106660. https://doi.org/10.1016/j.pepi.2021.106660

Baker, C., Hatzfeld, D., Lyon-Caen, H., Papadimitriou, E., & Rigo, A. (1997). Earthquake mechanisms of the Adriatic Sea and western Greece: Implications for the oceanic subduction-continental collision transition. *Geophysical Journal International*, *131*(3), 559–594. https://doi.org/10.1111/j.1365-246x.1997.tb06600.x

Behrens, J., Løvholt, F., Jalayer, F., Lorito, S., Salgado-Gálvez, M. A., Sørensen, M., et al. (2021). Probabilistic tsunami hazard and risk analysis: A review of research gaps. *Frontiers in Earth Science*, *9*, 628–772. https://doi.org/10.3389/feart.2021.628772

Bernard, P., Briole, P., Meyer, B., Lyon-Caen, H., Gomez, J.-M., Tiberi, C., et al. (1997). The M$_s$=6.2, June 15, 1995 Aigion earthquake (Greece): Evidence for low angle normal faulting in the Corinth rift. *Journal of Seismology*, *1*(2), 131–150. https://doi.org/10.1023/a:1009795618839

Bohnhoff, M., Rische, M., Meier, T., Becker, D., Stavrakakis, G., & Harjes, H. (2006). Microseismic activity in the Hellenic volcanic arc, Greece, with emphasis on the seismotectonic setting of the Santorini-Amorgos zone. *Tectonophysics*, *423*(1–4), 17–33. https://doi.org/10.1016/j.tecto.2006.03.024

Bondár, I., Engdahl, E. R., Villaseñor, A., Harris, J., & Storchak, D. (2015). ISC-GEM: Global instrumental earthquake catalogue (1900–2009), II. Location and seismicity patterns. *Physics of the Earth and Planetary Interiors*, *239*, 2–13. https://doi.org/10.1016/j.pepi.2014.06.002

Brüstle, A., Friederich, W., Meier, T., & Gross, C. (2014). Focal mechanism and depth of the 1956 Amorgos twin earthquakes from waveform matching of analogue seismograms. *Solid Earth*, *5*(2), 1027–1044. https://doi.org/10.5194/se-5-1027-2014

Davies, R., England, P., Parsons, B., Billiris, H., Paradissis, D., & Veis, G. (1997). Geodetic strain of Greece in the interval 1892–1992. *Journal of Geophysical Research*, *102*(B11), 24571–24588. https://doi.org/10.1029/97jb01644

Dziewonski, A. M., Chou, T.-A., & Woodhouse, J. H. (1981). Determination of earthquake source parameters from waveform data for studies of global and regional seismicity. *Journal of Geophysical Research*, *86*(B4), 2825–2852. https://doi.org/10.1029/jb086ib04p02825

Ekström, G., & Dziewonski, A. M. (1988). Evidence of bias in estimations of earthquake size. *Nature*, *332*(6162), 319–323. https://doi.org/10.1038/332319a0

Ekström, G., Nettles, M., & Dziewonski, A. (2012). The global CMT project 2004–2010: Centroid-moment tensors for 13,017 earthquakes. *Physics of the Earth and Planetary Interiors*, *200–201*, 1–9. https://doi.org/10.1016/j.pepi.2012.04.002

Elliott, J. R., Walters, R. J., England, P. C., Jackson, J. A., Li, Z., & Parsons, B. (2010). Extension on the Tibetan plateau: Recent normal faulting measured by InSAR and body wave seismology. *Geophysical Journal International*, *183*(2), 505–535. https://doi.org/10.1111/j.1365-246x.2010.04754.x

EMODnet. (2022). European marine observation and data network (EMODnet). Retrieved from https://emodnet.ec.europa.eu/en

Farr, T., Rosen, P., Caro, E., Crippen, R., Duren, R., Hensley, S., et al. (2007). The shuttle radar topography mission. *Reviews of Geophysics*, *45*(2), RG2004. https://doi.org/10.5066/F7PR7TFT

Feng, X., Ma, J., Zhou, Y., England, P., Parsons, B., Rizza, M. A., & Walker, R. T. (2020). Geomorphology and paleoseismology of the Weinan Fault, Shaanxi, Central China, and the source of the 1556 Huaxian earthquake. *Journal of Geophysical Research: Solid Earth*, *125*(12), e2019JB017848. https://doi.org/10.1029/2019JB017848

Galanopoulos, A. (1957). The seismic sea wave of 9 July 1956. *Praktika tes Akademias Athenon*, *32*, 90–101.

Ganas, A., Chousianitis, K., Batsi, E., Kolligri, M., Agalos, A., Chouliaras, G., & Makropoulos, K. (2012). The January 2010 Efpalion earthquakes (Gulf of Corinth, Central Greece): Earthquake interactions and blind normal faulting. *Journal of Seismology*, *17*(2), 1–20. https://doi.org/10.1007/s10950-012-9331-6

Ganas, A., Elias, P., Kapetanidis, V., Valkaniotis, S., Briole, P., Kassaras, I., et al. (2019). The July 20, 2017 M6.6 Kos earthquake: Seismic and geodetic evidence for an active north-dipping normal fault at the western end of the Gulf of Gökova (SE Aegean Sea). *Pure and Applied Geophysics*, *176*(10), 4177–4211. https://doi.org/10.1007/s00024-019-02154-y

GEBCO Compilation Group. (2024). GEBCO 2024 grid. https://doi.org/10.5285/1c44ce99-0a0d-5f4f-e063-7086abc0ea0f

Glimsdal, S., Pedersen, G. K., Harbitz, C. B., & Løvholt, F. (2013). Dispersion of tsunamis: Does it really matter? *Natural Hazards and Earth System Sciences*, *13*(6), 1507–1526. https://doi.org/10.5194/nhess-13-1507-2013

Green, G. (1838). On the motion of waves in a variable canal of small depth and width. *Transactions of the Cambridge Philosophical Society*, *6*, 223–230. https://doi.org/10.1017/cbo9781107325074.007

Hatzfeld, D., Karakostas, V., Ziazia, M., Kassaras, I., Papadimitriou, E., Makropoulos, K., et al. (2000). Microsesmicity and faulting geometry in the Gulf of Corinth (Greece). *Geophysical Journal International*, *141*(2), 438–456. https://doi.org/10.1046/j.1365-246x.2000.00092.x

Hatzfeld, D., Karakostas, V., Ziazia, M., Selvaggi, G., Leborgne, S., Berge, C., et al. (1997). The Kozani-Grevena (Greece) earthquake of 13 May 1995 revisited from a detailed seismological study. *Bulletin of the Seismological Society of America*, *87*(2), 463–473. https://doi.org/10.1785/bssa0870020463

Hatzfeld, D., Nord, J., Paul, A., Guiguet, R., Briole, P., Ruegg, J.-C., et al. (1995). The Kozani–Grevena (Greece) earthquake of May 13, 1995, M_s=6.6. Preliminary results of a field multidisciplinary survey. *Seismological Research Letters*, *66*(6), 61–70. https://doi.org/10.1785/gssrl.66.6.61

Hébert, H., & Schindelé, F. (2015). Tsunami impact computed from offshore modeling and coastal amplification laws: Insights from the 2004 Indian ocean tsunami. *Pure and Applied Geophysics*, *172*(12), 3385–3407. https://doi.org/10.1007/s00024-015-1136-4

Henry, C., & Das, S. (2001). Aftershock zones of large shallow earthquakes: Fault dimensions, aftershock area expansion and scaling relations. *Geophysical Journal International*, *147*(2), 272–293. https://doi.org/10.1046/j.1365-246X.2001.00522.x

Hooft, E. E. E., Nomikou, P., Toomey, D. R., Lampridou, D., Getz, C., Christopoulou, M.-E., et al. (2017). Backarc tectonism, volcanism, and mass wasting shape seafloor morphology in the Santorini-Christiana-Amorgos region of the Hellenic Volcanic Arc. *Tectonophysics*, *712–713*, 396–414. https://doi.org/10.1016/j.tecto.2017.06.005

Jackson, J. A., Gagnepain, J., Houseman, G., King, G. C. P., Papadimitriou, P., Soufleris, C., & Virieux, J. (1982). Seismicity, normal faulting, and the geomorphological development of the Gulf of Corinth (Greece): The Corinth earthquakes of February and March 1981. *Earth and Planetary Science Letters*, *57*(2), 377–397. https://doi.org/10.1016/0012-821x(82)90158-3

Johnson, K. L., Nissen, E., & Lajoie, L. (2018). Surface rupture morphology and vertical slip distribution of the 1959 Mw7.2 Hebgen Lake (Montana) earthquake from airborne lidar topography. *Journal of Geophysical Research: Solid Earth*, *123*(9), 8229–8248. https://doi.org/10.1029/2017jb015039

Kalligeris, N., Synolakis, C., England, P., Jackson, J., & Walker, R. (2025). Supporting information for implications of the 1956 July 9th M_S~7.2 Amorgos earthquake for tsunami hazard in the Aegean [Dataset]. *Geophysical Research Letters. American Geophysical Union*. https://doi.org/10.5281/zenodo.15623822

Karakostas, V., Tan, O., Kostoglou, A., Papadimitriou, E., & Bonatis, P. (2021). Seismotectonic implications of the 2020 Samos, Greece, Mw 7.0 mainshock based on high-resolution aftershock relocation and source slip model. *Acta Geophysica*, *69*(3), 979–996. https://doi.org/10.1007/s11600-021-00580-y

Karasözen, E., Nissen, E., Büyükakpınar, P., Cambaz, M. D., Kahraman, M., Kalkan Ertan, E., et al. (2018). The 2017 July 20 Mw 6.6 Bodrum–Kos earthquake illuminates active faulting in the Gulf of Gökova, SW Turkey. *Geophysical Journal International*, *214*(1), 185–199. https://doi.org/10.1093/gji/ggy114

Kassaras, I., Kapetanidis, V., Ganas, A., Karakonstantis, A., Papadimitriou, P., Kaviris, G., et al. (2022). Seismotectonic analysis of the 2021 Damasi-Tyrnavos (Thessaly, Central Greece) earthquake sequence and implications on the stress field rotations. *Journal of Geodynamics*, *150*, 101–898. https://doi.org/10.1016/j.jog.2022.101898

Kassaras, I., Kapetanidis, V., Karakonstantis, A., Kaviris, G., Papadimitriou, P., Voulgaris, N., et al. (2014). The April–June 2007 Trichonis lake earthquake swarm (W. Greece): New implications toward the causative fault zone. *Journal of Geodynamics*, *73*, 60–80. https://doi.org/10.1016/j.jog.2013.09.004

Leclerc, F., Palagonia, S., Feuillet, N., Nomikou, P., Lampridou, D., Barrière, P., et al. (2024). Large seafloor rupture caused by the 1956 Amorgos Tsunamigenic earthquake, Greece. *Communications Earth & Environment*, *5*(1), 663. https://doi.org/10.1038/s43247-024-01839-0

Lentas, K., Gkarlaouni, C. G., Kalligeris, N., & Melis, N. S. (2022). The 30 October 2020, M_w=7.0, Samos earthquake: Aftershock relocation, slip model, Coulomb stress evolution and estimation of shaking. *Bulletin of Earthquake Engineering*, *20*(2), 819–851. https://doi.org/10.1007/s10518-021-01260-4

Leonard, M. (2014). Self-consistent earthquake fault-scaling relations: Update and extension to stable continental strike-slip faults. *Bulletin of the Seismological Society of America*, *104*(6), 2953–2965. https://doi.org/10.1785/0120140087

Meyer, B., Armijo, R., Massonnet, D., de Chabalier, J. B., Delacourt, C., Ruegg, J. C., et al. (1996). The 1995 Grevena (northern Greece) earthquake: Fault model constrained with tectonic observations and SAR interferometry. *Geophysical Research Letters*, *23*(19), 2677–2680. https://doi.org/10.1029/96gl02389

Nomikou, P., Hübscher, C., Papanikolaou, D., Farangitakis, G. P., Ruhnau, M., & Lampridou, D. (2018). Expanding extension, subsidence and lateral segmentation within the Santorini - Amorgos basins during Quaternary: Implications for the 1956 Amorgos events, central - South Aegean Sea, Greece. *Tectonophysics*, *722*, 138–153. https://doi.org/10.1016/j.tecto.2017.10.016

Okada, Y. (1992). Internal deformation due to shear and tensile faults in a half-space. *Bulletin of the Seismological Society of America*, *82*(2), 1018–1040. https://doi.org/10.1785/bssa0820021018

Okal, E. A., Synolakis, C. E., Uslu, B., Kalligeris, N., & Voukouvalas, E. (2009). The 1956 earthquake and tsunami in Amorgos, Greece. *Geophysical Journal International*, *178*(3), 1533–1554. https://doi.org/10.1111/j.1365-246x.2009.04237.x

Papadopoulos, G., & Pavlides, S. (1992). The large 1956 earthquake in the South Aegean: Macroseismic field configuration, faulting, and neotectonics of Amorgos island. *Earth and Planetary Science Letters*, *113*(3), 383–396. https://doi.org/10.1016/0012-821x(92)90140-q

Resor, P. G., Pollard, D. D., Wright, T. J., & Beroza, G. C. (2007). Integrating high-precision aftershock locations and geodetic observations to model coseismic deformation associated with the 1995 Kozani-Grevena earthquake, Greece. *Journal of Geophysical Research*, *110*(B9), B09402. https://doi.org/10.1029/2004jb003263

Satake, K., Ishibe, T., Murotani, S., Mulia, I. E., & Gusman, A. R. (2022). Effects of uncertainty in fault parameters on deterministic tsunami hazard assessment: Examples for active faults along the eastern margin of the sea of Japan. *Earth Planets and Space*, *74*(1), 36. https://doi.org/10.1186/s40623-022-01594-6

Savage, J., & Hastie, L. (1966). Surface deformation associated with dip-slip faulting. *Journal of Geophysical Research*, *71*(20), 4897–4904. https://doi.org/10.1029/jz071i020p04897

Selva, J., Lorito, S., Volpe, M., Romano, F., Tonini, R., Perfetti, P., et al. (2021). Probabilistic tsunami forecasting for early warning. *Nature Communications*, *12*(1), 5677. https://doi.org/10.1038/s41467-021-25815-w

Shaw, B., & Jackson, J. (2010). Earthquake mechanisms and active tectonics of the Hellenic subduction zone. *Geophysical Journal International*, *181*, 966–984. https://doi.org/10.1111/j.1365-246x.2010.04551.x

Shaw, B. E., & Scholz, C. H. (2001). Slip-length scaling in large earthquakes: Observations and theory and implications for earthquake physics. *Geophysical Research Letters*, *28*(15), 2995–2998. https://doi.org/10.1029/2000GL012762

Stiros, S., Marangou, L., & Arnold, M. (1994). Quaternary uplift and tilting of Amorgos Island (southern Aegean) and the 1956 earthquake. *Earth and Planetary Science Letters*, *128*, 65–76. https://doi.org/10.1016/0012-821X(94)90135-X

Synolakis, C. E. C., & Okal, E. A. (2005). 1992–2002: Perspective on a decade of post-tsunami surveys, chap. In *Tsunamis: Case studies and recent developments* (pp. 1–29). Springer.

Taymaz, T., Jackson, J., & McKenzie, D. (1991). Active tectonics of the north and central Aegean Sea. *Geophysical Journal International*, *106*(2), 433–490. https://doi.org/10.1111/j.1365-246x.1991.tb03906.x

Titov, V. V., Kânoğlu, U., & Synolakis, C. (2016). Development of MOST for real-time tsunami forecasting. *Journal of Waterway, Port, Coastal, and Ocean Engineering*, *142*(6), 03116004. https://doi.org/10.1061/(ASCE)WW.1943-5460.0000357

Titov, V. V., & Synolakis, C. (1998). Numerical modeling of tidal wave runup. *Journal of Waterway, Port, Coastal, and Ocean Engineering*, *124*(4), 157–171. https://doi.org/10.1061/(asce)0733-950x(1998)124:4(157)

Titov, V. V., Moore, C. W., Greenslade, D. J. M., Pattiaratchi, C., Badal, R., Synolakis, C. E., & Kânoğlu, U. (2011). A new tool for inundation modeling: Community modeling interface for tsunamis (ComMIT). *Pure and Applied Geophysics*, *168*(11), 2121–2131. https://doi.org/10.1007/s00024-011-0292-4

Titov, V. V., & Synolakis, C. E. (1995). Modeling of breaking and nonbreaking long-wave evolution and runup using VTCS-2. *Journal of Waterway, Port, Coastal, and Ocean Engineering*, *121*(6), 308–316. https://doi.org/10.1061/(ASCE)0733-950X(1995)121:6(308)

Tsampouraki-Kraounaki, K., Sakellariou, D., Rousakis, G., Morfis, I., Panagiotopoulos, I., Livanos, I., et al. (2021). The Santorini-Amorgos shear zone: Evidence for Dextral transtension in the South Aegean back-arc region, Greece. *Geosciences*, *11*(5), 216. https://doi.org/10.3390/geosciences11050216

UNESCO-IOC. (2019). UNESCO tsunami glossary. Retrieved from https://unesdoc.unesco.org/ark:/48223/pf0000188226

Walker, R. T., Wegmann, K. W., Bayasgalan, A., Carson, R. J., Elliott, J., Fox, M., et al. (2017). The Egiin Davaa prehistoric rupture, central Mongolia: A large magnitude normal faulting earthquake on a reactivated fault with little cumulative slip located in a slowly deforming intraplate setting. *Geological Society, London, Special Publications*, *432*(1), 187–212. https://doi.org/10.1144/SP432.4

Wells, D., & Coppersmith, K. (1994). New empirical relationships among magnitude, rupture length, rupture width, rupture area, and surface displacement. *Bulletin of the Seismological Society of America*, *84*(4), 974–1002. https://doi.org/10.1785/bssa0840040974

Wessel, P., Smith, W. H. F., Scharroo, R., Luis, J., & Wobbe, F. (2013). Generic mapping tools: Improved version released. *Eos, Transactions, American Geophysical Union*, *94*(45), 409–410. https://doi.org/10.1002/2013eo450001

References From the Supporting Information

Ambraseys, N. N. (2009). *Earthquakes in the Mediterranean and Middle East*. Cambridge University Press.

Giacomo, D. D., Bondár, I., Storchak, D. A., Engdahl, E. R., Bormann, P., & Harris, J. (2015). ISC-GEM: Global instrumental earthquake catalogue (1900–2009), III. Re-computed MS and mb, proxy MW, final magnitude composition and completeness assessment. *Physics of the Earth and Planetary Interiors*, *239*, 33–47. https://doi.org/10.1016/j.pepi.2014.06.005

Hartl, H. (1911). Griechenland: Bericht über Drieeckmessungen. In *Comptes Rendus de la Seizème Conférence Générale de l'Association Géodèsique Internationale*. Assoc. Géod. Int.

Howell, A., Jackson, J., Copley, A., Mckenzie, D., & Nissen, E. (2017). Subduction and vertical coastal motions in the eastern Mediterranean. *Geophysical Journal International*, *211*(1), 593–620. https://doi.org/10.1093/gji/ggx307

Jackson, J., & McKenzie, D. (2022). The exfoliation of cratonic Australia in earthquakes. *Earth and Planetary Science Letters*, *578*, 117–305. https://doi.org/10.1016/j.epsl.2021.117305

Kiratzi, A., & Louvari, E. (2003). Focal mechanisms of shallow earthquakes in the Aegean Sea and the surrounding lands determined by waveform modelling: A new database. *Journal of Geodynamics*, *36*(1–2), 251–274. https://doi.org/10.1016/S0264-3707(03)00050-4

Lee, W. H. K., & Engdahl, E. R. (2015). Bibliographical search for reliable seismic moments of large earthquakes during 1900–1979 to compute MW in the ISC-GEM global instrumental reference earthquake catalogue. *Physics of the Earth and Planetary Interiors*, *239*, 25–32. https://doi.org/10.1016/j.pepi.2014.06.004